ADVANCED MATERIALS
www.advmat.de

Bioinspired Multifunctional Photonic-Electronic Smart Skin for Ultrasensitive Health Monitoring, for Visual and Self-Powered Sensing

Yi Zhao, Wenchao Gao, Kun Dai, Shuo Wang, Zuqing Yuan, Jiannan Li, Wei Zhai, Guoqiang Zheng, Caofeng Pan,* Chuntai Liu,* and Changyu Shen*

Smart skin is highly desired to be ultrasensitive and self-powered as the medium of artificial intelligence. Here, an ultrasensitive self-powered mechanoluminescence smart skin (SPMSS) inspired by the luminescence mechanism of cephalopod skin and the ultrasensitive response of spider-slit-organ is developed. Benefitting from the unique strain-dependent microcrack structure design based on $Ti_3C_2T_x$ (MXene)/carbon nanotube synergistic interaction, SPMSS possesses excellent strain sensing performances including ultralow detection limit (0.001% strain), ultrahigh sensitivity (gauge factor, GF = 3.92×10^7), ultrafast response time (5 ms), and superior durability and stability (>45 000 cycles). Synchronously, SPMSS exhibits tunable and highly sensitive mechanoluminescence (ML) features under stretching. A relationship between ML features, strain sensing performances, and the deformation has been established successfully. Importantly, the SPMSS demonstrates excellent properties as triboelectric nanogenerator (4×4 cm^2), including ultrahigh triboelectric output (open-circuit voltage V_{OC} = 540 V, short-circuit current I_{SC} = 42 µA, short-circuit charge Q_{SC} = 317 nC) and power density (7.42 W m^{-2}), endowing the smart skin with reliable power source supply and self-powered sensing ability. This bioinspired smart skin exhibits multifunctional applications in health monitoring, visual sensing, and self-powered sensing, showing great potential in artificial intelligence.

1. Introduction

Recently, smart skin as the medium of artificial intelligence (AI), soft robots, and health monitors has received great attention.[1] With overwhelming development of these key fields, it is vital to develop smart and interactive electronics with multi-functions.[2] Generally, smart skin is expected to be ultrasensitive,[3] self-powered,[4] and it is desirable to endow the skin with the ability to sense stimuli visually.[5]

In recent years, several smart skins based on $Ti_3C_2T_x$ (MXene)-strain/pressure sensors have been developed to achieve fascinating sensing performances such as high sensitivity, low detection limit, and good repeatable stability.[6,7] However, the trade-off between these sensing abilities and the oxidation phenomenon of MXene[8] in devices have greatly limited the applications of these smart skins. Eidetic signal recognition of smart skin, such as color or luminance, has become important for the development of AI and health fields. Mechanoluminescence (ML), which can change the color or luminance under varying deformation, has great potential in delicate urgent medical or safety-related industries by visualization of mechanical signals.[9] Moreover, reliable and sustainable power supply is essential for smart skin in practical applications. Recently, triboelectric nanogenerator (TENG), converting mechanical energy into electricity by contact electrification and electrostatic induction, has been proved to possess good application prospect in energy harvesting and self-powered sensing.[10] It is still a great challenge to prepare an all-in-one smart skin intrinsically integrating the properties as mentioned above, such as, excellent sensing ability, tunable optical characteristics, and reliable power supply.

Here, we developed an ultrasensitive self-powered ML smart skin (SPMSS) that demonstrated health monitoring, visual and the self-powered sensing (**Figure 1**a). The bioinspired strain-dependent microcrack structure was designed by spraying 1D carbon nanotube (CNT)/2D MXene conductive ink on electrospun thermoplastic polyurethane (TPU) fluorescent

Y. Zhao, Prof. K. Dai, S. Wang, J. Li, W. Zhai, Prof. G. Zheng, Prof. C. Liu, Prof. C. Shen
School of Materials Science and Engineering
Key Laboratory of Materials Processing and Mold
Ministry of Education
Zhengzhou University
Zhengzhou 450001, P. R. China
E-mail: kundai@zzu.edu.cn; ctliu@zzu.edu.cn

Y. Zhao, Dr. Z. Yuan, Prof. C. Pan
CAS Center for Excellence in Nanoscience
Beijing Key Laboratory of Micro-nano Energy and Sensor
Beijing Institute of Nanoenergy and Nanosystems
Chinese Academy of Sciences
Beijing 100083, P. R. China
E-mail: cfpan@binn.cas.cn

Dr. W. Gao
Department of Civil Engineering
Monash University
Clayton 3800, Australia

The ORCID identification number(s) for the author(s) of this article can be found under https://doi.org/10.1002/adma.202102332.

DOI: 10.1002/adma.202102332

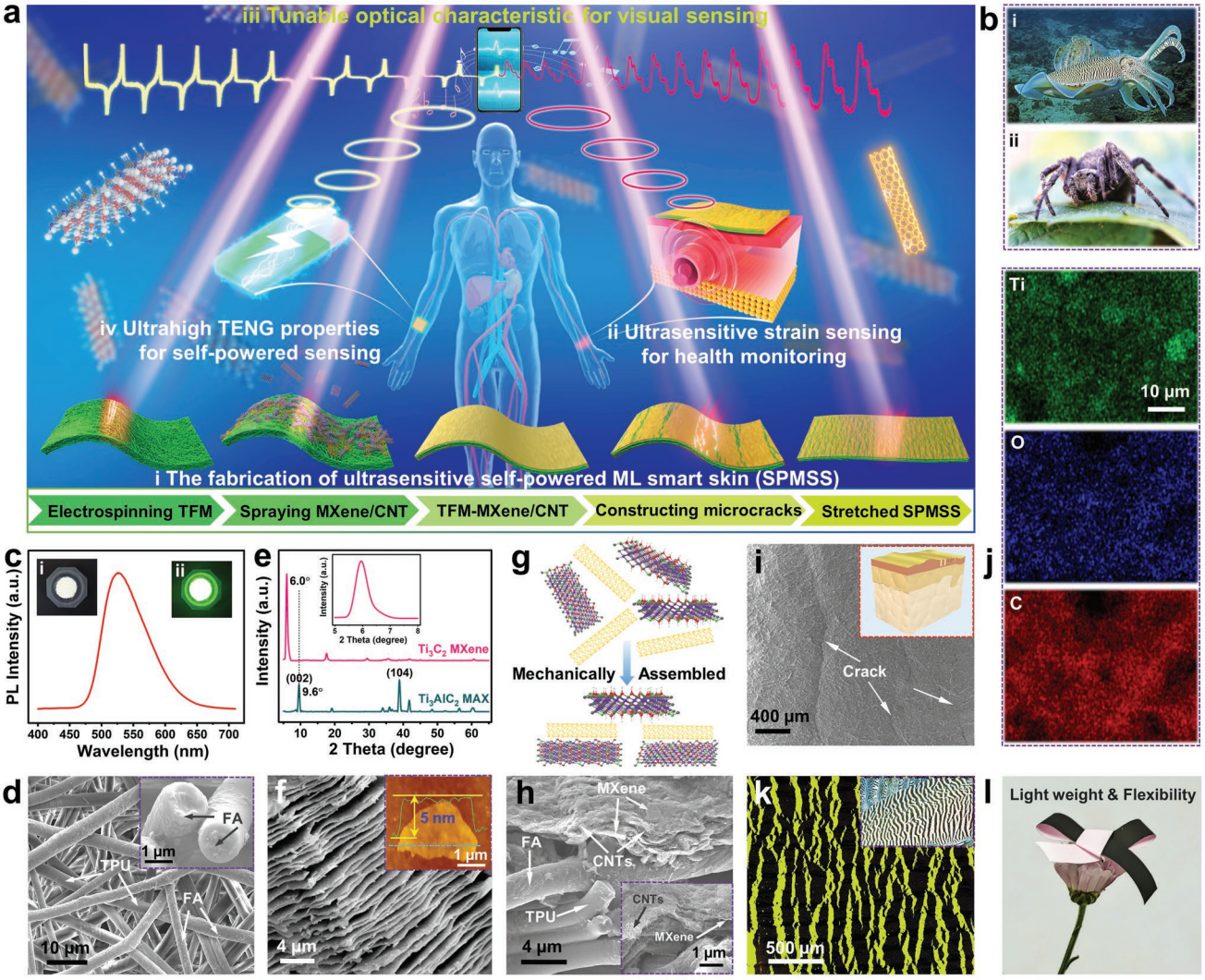

Figure 1. Material structure design. a) Schematic illustration of the fabrication and application of SPMSS. b) i) Luminescence mechanism of cephalopod skin and ii) ultrasensitive response of a spider-slit-organ. c) PL spectra of the FA. The inset shows FA powder at i) daylight and ii) 365 nm UV light. d) Scanning electron microscopy (SEM) image of TFM with 4% FA. The inset is the cross-sectional SEM image. e) X-ray diffraction (XRD) patterns of MAX precursor and MXene nanosheets with inset of the magnified XRD pattern at low Bragg angles. f) SEM image of multilayered MXene. The inset is atomic force microscope (AFM) image for MXene nanosheets. g) Schematic illustration of the assembly of MXene and CNT. h) Cross-sectional SEM image of SPMSS. The inset shows the morphology at a large magnification. i) SEM image of the surface of SPMSS. The inset is an enlarged diagram of spider-slit-organ. j) Element mapping images of Ti, C, and O elements in SPMSS. k) Optical microscopy images of SPMSS under stretching. The inset is an enlarged diagram of cephalopod skin. l) The optical image of a bowknot woven by SPMSS placed on a flower.

mat (TFM) and then constructing microcracks (Figure 1a-i). SPMSS possessed excellent sensing performances under stretching, such as ultralow detection limit (0.001% strain), ultrahigh sensitivity (gauge factor, GF = 3.92×10^7), ultrafast response time (5 ms), and superior durability and stability (>45 000 cycles). These excellent abilities enabled SPMSS to monitor pulses in different parts of human body accurately (Figure 1a-ii) and detect the gestures visually (Figure 1a-iii). The SPMSS exhibited superior TENG properties including an ultrahigh triboelectric output (open-circuit voltage V_{OC} = 540 V, short-circuit current I_{SC} = 42 μA, short-circuit charge Q_{SC} = 317 nC) and power density (7.42 W m^{-2}), endowing the smart skin with the capability of reliable power source supply and self-powered sensing (Figure 1a-iv). The multifunctional smart skin provides unique opportunities for wearable flexible electronics and AI.

2. Results and Discussions

In nature, animal skins exhibit a variety of intriguing functions to acclimatize and survive. For instance, some cephalopods, by adjusting exposure areas of the pigment sacs during radial muscle movement, can transform color or luminosity of their skin for the purpose of communication and camouflage (Figure 1b-i).[11] Spiders have crack-shaped slit organs to detect very small external stimuli for predation and concealment (Figure 1b-ii).[3] If these fascinating features can be successfully

applied to an all-in-one smart skin, it will significantly promote and extend the development of the electronic skins. Given this, we develop a multifunctional smart skin inspired by significant changes in fluorescence of cephalopod skin and the ultrasensitive response of spider-slit-organ.

The preparation of the smart skin is illustrated in Figure 1a-i. First, TPU was selected as substrate layer due to its flexibility, durability and biocompatibility, commercial fluorescent agent (FA) with low cost and high stability was used as efficient fluorescent material. The photoluminescence (PL) spectra of the FA (yellow light) is displayed in Figure 1c, showing a fixed characteristic peak of 527 nm and intense fluorescent emission under 365 nm ultraviolet (UV) light (Figure 1c-ii). The FAs with varying mass ratio of 0, 1, 2, 4, 8, and 12% were mixed with TPU to prepare a series of TFMs through electrospinning. By comparing the fluorescence properties (Figure S1a–c, Supporting Information) and mechanical properties (Figure S1d, Supporting Information) of TFM with different FA contents, we find 4% TFM possesses both excellent fluorescent performance and superior stretchability (792% strain) (Figure S1e,f, Supporting Information). FA is evenly distributed on the surface and inside the fiber, and the fibers are well overlapped with each other, forming a good porous network structure (Figure 1d and Figures S2 and S3, Supporting Information). Conductive MXene nanosheets were prepared through selectively etching of MAX phase (Ti_3AlC_2) (Figure S4, Supporting Information).[12] The successful preparation of 2D MXene nanosheets is validated by the shift of X-ray diffraction peak (002) from 9.6° to 6.0° and the disappearance of the most intense diffraction peak of Ti_3AlC_2 at 39° (Figure 1e).[7c] As shown in Figure S5a, Supporting Information, and Figure 1f, Ti_3AlC_2 has changed into MXene with a loosely stacked accordion-like multilayer structure after etching; the delaminated MXene nanosheets exhibit an ultrathin structure with a thickness of ≈5 nm (in inset) and a lateral size around 2 to 3 µm (Figure S5b, Supporting Information). Moreover, in Raman spectrum (Figure S6a, Supporting Information), the A_{1g} symmetry out-of-plane vibrations of Ti and C atoms generate the peaks at 198 and 717 cm^{-1}, respectively; the peaks at 284, 366, and 624 cm^{-1} attribute to the E_g group vibrations composed of in-plane (shear) modes of Ti, C, and surface functional group atoms, respectively.[13] The X-ray photoelectron spectroscopy (XPS) spectra exhibit that the MXene mainly contains elements of Ti, C, O, and F (Figure S6b–f, Supporting Information). The energy-dispersive X-ray spectroscopy elemental mapping analyses indicate that the main elements (Ti, C) and surface terminations (O, OH, and F) of the MXene are distributed uniformly (Figure S7, Supporting Information).

In order to enhance the electrical properties, as shown in Figure S8, Supporting Information, and Figure 1g, stable CNT ink was chose to be assembled with MXene. SPMSS was then built by spraying 1D CNT/2D MXene conductive ink on 4% TFM, microcracks structure was then constructed by pre-treatment (Figure S9, Supporting Information). In Figure S10, Supporting Information, and Figure 1h, the cross-sectional SEM image of SPMSS exhibits a good sandwich structure by tightly wrapping MXene sheets with CNT ink, multiscale jagged microcracks like the spider-slit-organ is obtained after pre-treatment (Figure 1i), MXene/CNT are distributed uniformly on the surface of SPMSS (Figure 1j). SPMSS displays tunable ML characteristic under stretching based on the strain-dependent microcrack-structure like cephalopod skin (in inset) (Figure 1k), and exhibits light-weight feature and good flexibility (Figure 1l).

The electromechanical properties of SPMSS with different MXene/CNT contents are characterized by detecting the relative resistance change ($\Delta R/R_0$, $\Delta R = R\text{-}R_0$, R_0 represents the original resistance, R stands for the resistance under strain). As shown in Figure S11a, Supporting Information, MXene/CNT content of 1:1 endows SPMSS with a wider sensing range and higher sensitivity compared to the samples with other contents. Typical $\Delta R/R_0$-strain curve and stress–strain curve of SPMSS with MXene/CNT content of 1:1 are studied in detail in Figure S11b, Supporting Information. **Figure 2**a shows the different sensitivities in three distinct strain stages (region I from 0 to 25%, II from 25 to 50%, and III from 50 to 65%). The sensitivity is evaluated by using the indicator GF:[14]

$$GF = \frac{\Delta R/R_0}{\varepsilon} \tag{1}$$

where ε represents the strain. It is worth noting that SPMSS possesses an ultrahigh GF of 8.05×10^5 in region I, 9.36×10^6 in region II, and 3.92×10^7 in region III, which is one of the highest reported sensitivities in available literatures (Figure 2b).[3,6c,15–17] To validate the detection limit of SPMSS, as shown in Figure 2c, a series of cyclic sensing behaviors toward ultralow strains of 0.001%, 0.005%, 0.01%, 0.05%, 0.1%, 0.5%, and 1% are performed. Obviously, even at an ultralow strain of 0.001%, stable response signals can be accurately obtained. A very fast response/recovery time of 5 ms is achieved at a stretching speed of 1000 mm min^{-1} (Figure 2d). In Figure 2f, compared with other recent available reports, SPMSS possesses one of the lowest detection limit and the fastest response time.[6d,15a,c,17b,18–20]

SPMSS exhibits good stability and durability (>1000 cycles) even under an ultralow strain of 0.05% (Figure S12, Supporting Information). These results benefit from the unique microcrack-structure and the synergistic effect between 1D CNTs and 2D MXene, which ensures excellent sensing response to deformations in real time. Furthermore, Figure 2e exhibits remarkable long-term durability and stability after 45 000 stretching-releasing cycles under a larger strain of 5%. Figure S13, Supporting Information, shows that SPMSS has excellent stability and standard Ohm behavior under 0–50% strains. Stretching rates have negligible effect on the sensing performance of SPMSS (Figure S14, Supporting Information,), which is of great significance for acquiring reliable response in practical applications.

Considering the crack structural evolution of SPMSS under different strains (Figure S15, Supporting Information), we understand the sensing mechanism in stretching. As shown in Figure 2g, the destruction of conductive network is mainly ascribed to the appearance of cracks toward stretching. Under a very small strain, 2D MXene flakes play a leading role, the number of contact points between neighboring 2D MXene flakes is reduced owing to the increase of crack size, and the electron transfer is hindered, showing a sensitive response. When the strain increases, more cracks are generated, the

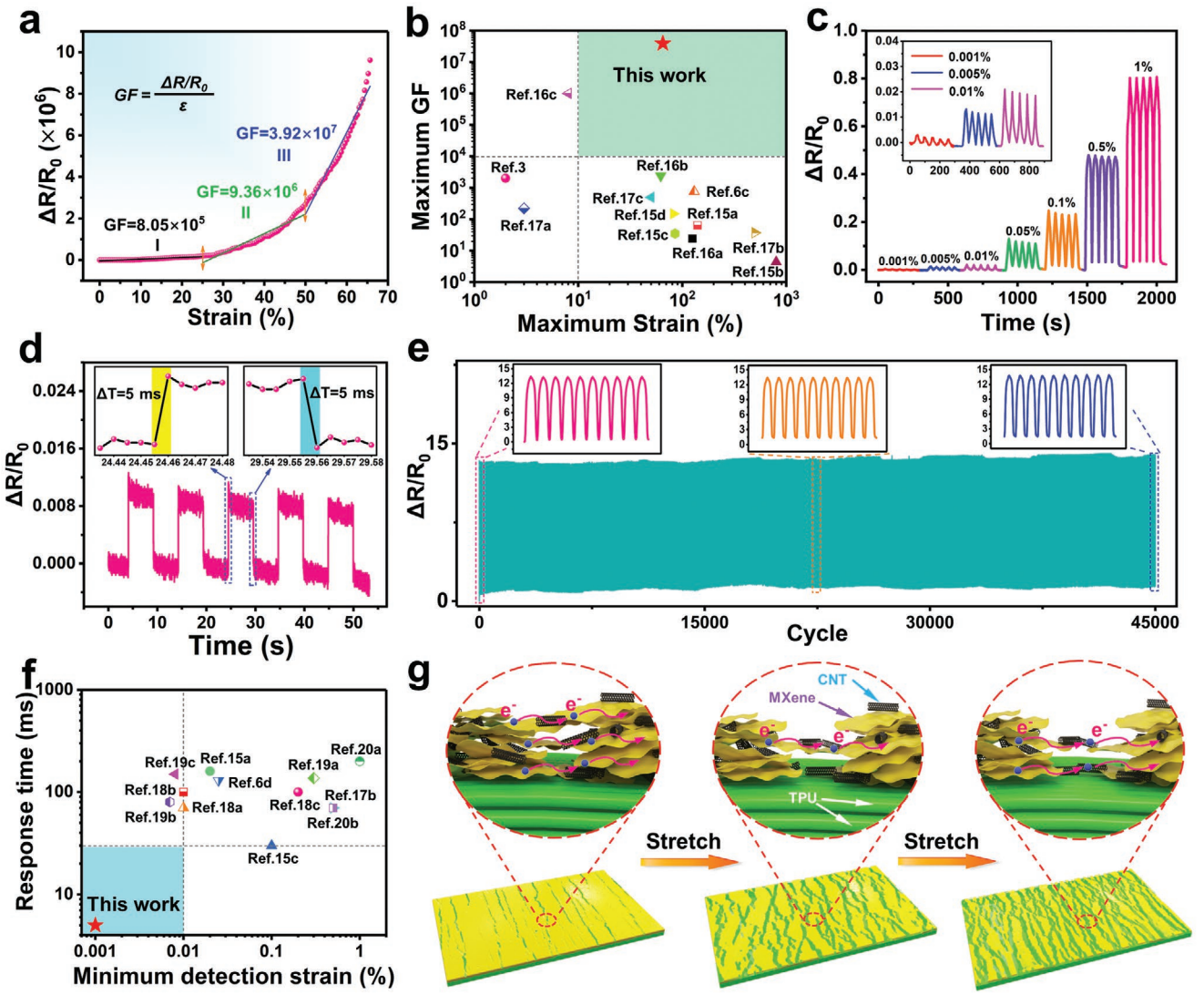

Figure 2. The strain sensing performances and mechanism of SPMSS. a) GF at various strains. b) Comparison of maximum GF and maximum strain range to recent literatures. c) $\Delta R/R_0$-strain curves at the strain of 0.001%, 0.005%, 0.01%, 0.05%, 0.1%, 0.5%, and 1%. d) Response and recovery time. e) Long-term stability during 45 000 cycles toward 5% strain. f) Comparison of detection strain limit and response time. g) Schematic of the crack propagation of SPMSS under stretching.

conductive pathways are continuously damaged, and higher resistance is observed gradually. When the strain is very large (50–65%), 1D CNT network as a bridge connects the divided MXene flakes, allowing the electrons to travel, giving the SPMSS with an ultrahigh GF and an enlarged sensing range due to contacts between CNTs and MXene on two edges of the microcracks. Here, the introduction of 2D MXene endows the sensor with an ultralow detection limit based on the susceptive contact between the nanosheets in the crack structure; 1D CNT acting as bridge benefits to the wide strain range and good sensing stability on the basis of the synergistic effect. In addition, sensing performances to bending that is always observed in human activities are also studied. As shown in Figure S16, Supporting Information, SPMSS shows favorable ability of bending sensing, including stable and identical response, high stability, and repeatability (>1000 cycles).

Benefitting from the unique strain-dependent microcrack-structure design based on MXene/CNT synergistic interaction, SPMSS exhibits rapidly reversible strain-dependent optical characteristic. As shown in Figure S17, Supporting Information, MXene/CNT conductive layer of SPMSS possesses good UV shielding abilities in the initial state. In **Figure 3**a, when SPMSS with yellow fluorescent color is stretched continuously, microcracks occur on the conductive layer with the evolution of the crack size, these microcracks as "gates" controllably regulate exposure region of TFM and the accompanied fluorescence intensity of SPMSS. As indicated in Figure 3b, no visible fluorescence is observed in the initial state due to good UV shielding abilities of MXene/CNT layer, the brightness of yellow fluorescence on SPMSS strengthens gradually as strain increases. As shown in Figure 3c, SPMSS based on different FA displays various fluorescence color (red, yellow,

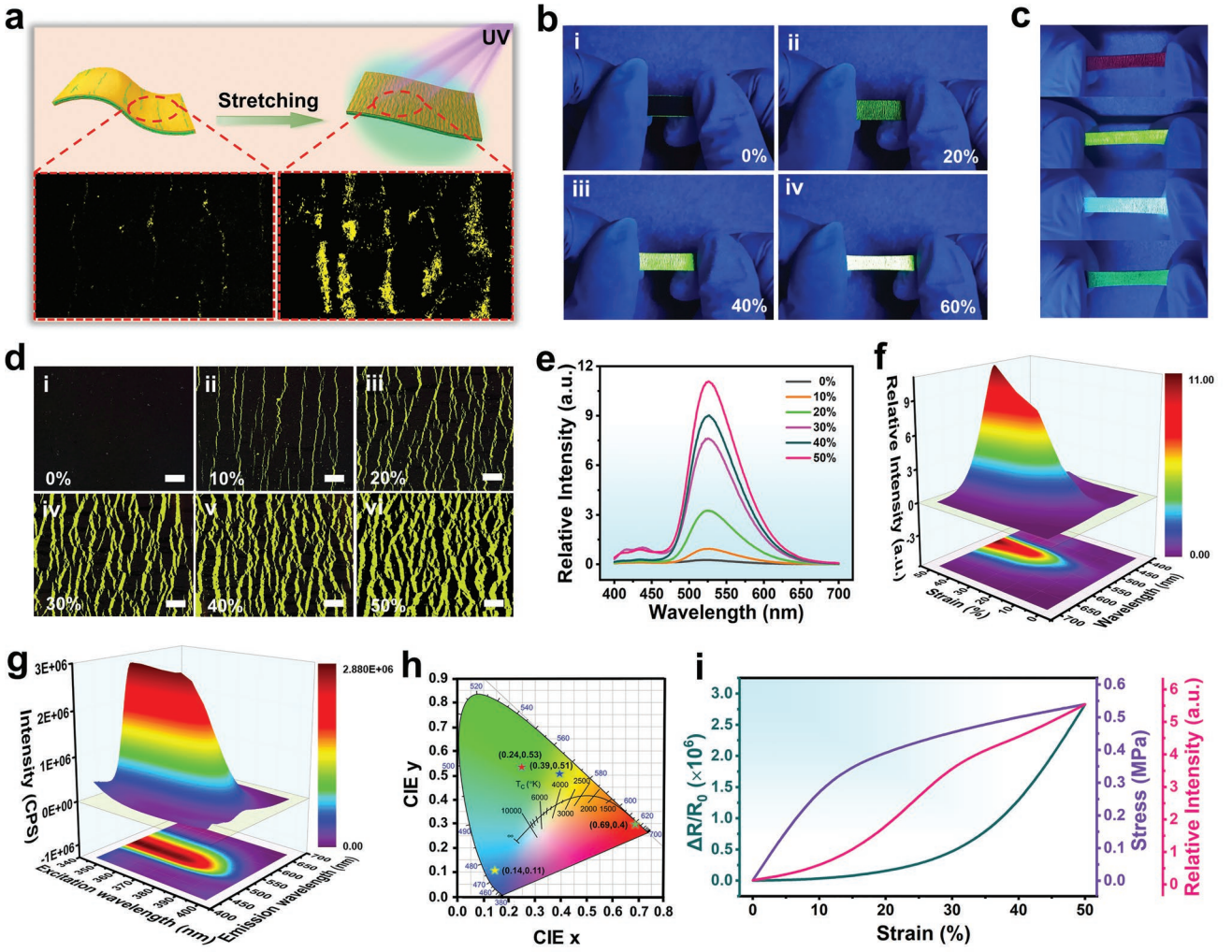

Figure 3. Tunable ML optical properties of SPMSS for visual sensing. a) Working mechanism of tunable ML, the insets are laser scanning confocal microscope images of different states. b) Fluorescent photographs of SPMSS with yellow fluorescent color under varying tensile strains. c) Photographs of SPMSS with different fluorescent colors (red, yellow, blue, and green) under stretching. d) Optical microscopy images of SPMSS with yellow fluorescent color at a series of strains (scale bars 500 μm). e,f) The ML spectra of SPMSS with yellow fluorescent color at varying strains. g) 3D emission fluorescence spectra of SPMSS with yellow fluorescent color before 1000 tensile cycles under 50% strain. h) CIE coordinates of SPMSS including different fluorescent colors. i) Stress, $\Delta R/R_0$ and fluorescent intensity–strain curves.

blue, and green) well under stretching (Figure S18, Supporting Information). Dynamical ML properties of SPMSS are exhibited in Video S1, Supporting Information, as the applied stress is released, SPMSS rapidly restores to the initial state and the bright fluorescence disappears simultaneously.

In Figure 3d, the microcracks on SPMSS are basically closed in releasing state i), the number and width of the microcracks, which are displayed as bright yellow-light areas ii–vi) under an optical microscope, become larger as the tensile strain increases. To quantitatively evaluate the strain-dependent luminescence intensity of SPMSS, the fluorescence spectra as a function of strain are also investigated. As shown in Figure 3e,f (i.e., Figure S19c,d for SPMSS with yellow fluorescent color) and Figure S19a,b,e–h, Supporting Information, the fluorescence intensity of SPMSS increases monotonously with increasing the applied tensile strain. Compared with initial fluorescent state, Figure 3g (i.e., Figure S20b for SPMSS with yellow fluorescent color) and Figures S20a,c,d and 21, Supporting Information, exhibit that 3D emission fluorescence spectra of SPMSS possess nearly uniform characteristic after 1000 stretching-releasing cycles under 50% strain, exhibiting desirable stability and durability. Figure 3h shows Commission International de L'Eclairage (CIE) coordinates of SPMSS with different fluorescent colors (red, yellow, blue, and green). Attributed to the unique strain-dependent microcrack structure, SPMSS can sense external stimuli in real-time through visually bright and colorful luminescence. As shown in Figure 3i, the visual sensing is realized through integrating $\Delta R/R_0$, stress and fluorescence intensity as a function of tensile strain. SPMSS displays the unique strain-dependent ML ability, possessing great potential in application of optical display and visual sensing.

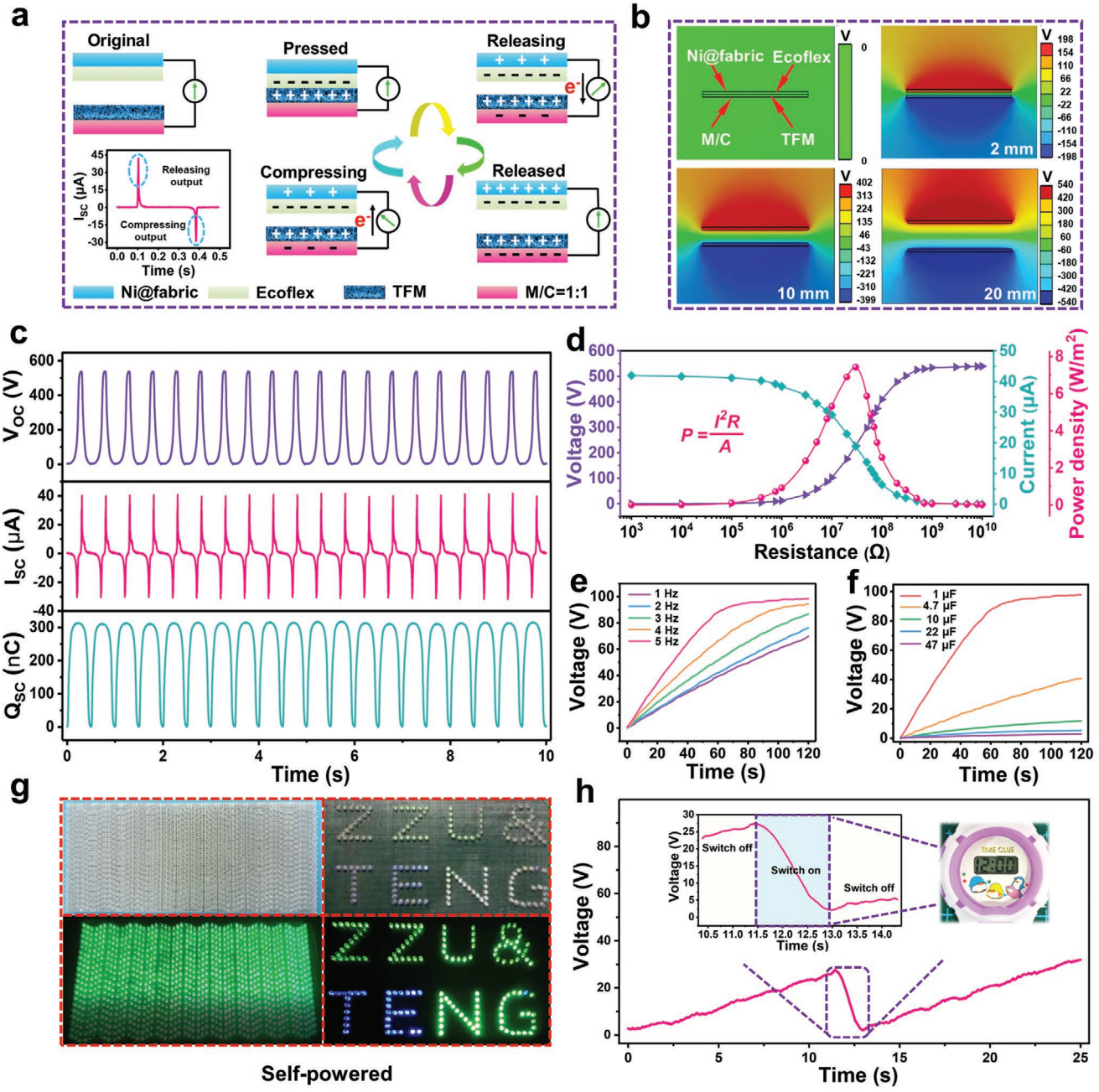

Figure 4. The TENG (4 × 4 cm^2) performances of SPMSS for energy harvesting. a) Working mechanism of SPMSS, M and C represent MXene and CNT, respectively. b) Finite element simulation of electric potential distribution of SPMSS. c) V_{OC}, I_{SC}, and Q_{SC} signals of SPMSS at applied pressure of 10 N and frequency 2 Hz. d) Measured output voltage, output current, and output power density with variable load resistances. e) Charging ability of SPMSS at different frequencies and f) capacitor capacities. g) Digital photographs of lighting LEDs. h) Reliable power source supply for driving an electronic watch by 1 μF capacitor.

On the basis of excellent electronic transmission of MXene/CNT conductive layer and strong electronegativity of TFM substrate layer with good roughness (R_a = 2.28 μm, in Figure S22, Supporting Information), SPMSS exhibits excellent TENG properties for energy harvesting and self-powered sensing. **Figure 4**a illustrates that SPMSS in two-electrode mode comprises of two parts: TFM and Ecoflex as triboelectric layers, MXene/CNT and Ni@fabric as electrode layer, respectively. The triboelectric working mechanism of SPMSS is similar to our previous report.[10d] Figure 4b presents the simulated electric potential distribution by finite element analysis, explaining the process of triboelectrification quantitatively. Figure 4c illustrates ultrahigh triboelectric output of SPMSS (4 × 4 cm^2) including the V_{OC} = 540 V, I_{SC} = 42 μA, and Q_{SC} = 317 nC, respectively. Figure 4d displays the measured output voltage, output current and output power density with variable load resistances

of 1 kΩ–10 GΩ. The output power density (P) is calculated according to the Equation (2) as follows:[21]

$$P = \frac{I^2 R}{A} \tag{2}$$

Here, R is loading resistance, A and I stand for the contact area and output current of SPMSS, respectively. Figure 4d exhibits that the maximum output power density is 7.42 W m^{-2} at a resistance of 30 MΩ, generating reliable power source supply. The circuit diagram of a self-powered system is established in Figure S23, Supporting Information, and SPMSS shows excellent charging ability at different frequencies (1–5 Hz) and capacitor capacities (1–47 μF) (Figure 4e,f). When tapping SPMSS based TENG with a hand, 1080 green light-emitting diodes (LEDs) and the letter-shaped LEDs (ZZU and TENG) can be easily lighted up (Figure 4g). Furthermore, as shown in Figure 4h, SPMSS achieves reliable power source supply for driving an electronic watch by charging the capacitor (1 μF). In conclusion, as a promising power provider, SPMSS can drive electronic products by harvesting energy, and it has a good practicability.

SPMSS (2 × 2 cm^2) also displays superior single-electrode TENG (S-TENG) properties, which can harvest biomechanical energy and self-powered sensing efficiently. Figure S24a,b, Supporting Information, show the structure of SPMSS in single-electrode mode and the great flexibility of SPMSS, respectively. As indicated in Figure S25, Supporting Information, working mechanism of SPMSS in single-electrode mode is similar to previous report.[10e] Simulated electric potential distribution in the triboelectric process by finite element analysis is demonstrated quantitatively (Figure S26, Supporting Information). V_{OC}, I_{SC}, and Q_{SC} of SPMSS measured at various applied pressures (at a constant frequency of 0.45 Hz) and various applied frequencies (at a constant pressure of 10 N) are shown in Figures S27 and S28a–c, Supporting Information, respectively. Figure S27d, Supporting Information, exhibits a good linear response of SPMSS with high pressure sensitivities of 3.443 mV kPa^{-1}, which is mainly attributed to the effective contact area between the frictional layers. As shown in Figure S27e, Supporting Information, when the applied pressure increases, the effective contact area between Ecoflex and TFM rises owing to the deformation of TPU fluorescence fiber and Ecoflex. A larger effective contact area leads to more charge accumulation, causing the increase in V_{OC}. These results indicate that SPMSS exhibits excellent response behaviors to different pressures and frequencies, which can be applied for self-powered tactile sensing. Figure S28d, Supporting Information, displays the output current and power density toward different load resistances, the largest P of 185 mW m^{-2} is achieved under an input resistance of 500 MΩ. Moreover, SPMSS shows an excellent stability even after 20 000 pressing-releasing cycles (Figure S29, Supporting Information).

In order to simultaneously realize strain sensing and signal visualization of SPMSS, real-time monitoring is demonstrated through integrating SPMSS on the finger of a volunteer as shown in **Figure 5**a,c. Figure 5a,b illustrate that the luminescent intensity and $\Delta R/R_0$ of SPMSS are simultaneously increased as the bending angle increases, providing the possibility for application in synchronously visual sensing for a robotic finger. Furthermore, Figure 5c shows an accurate response of $\Delta R/R_0$ and luminescent effect to different gestures, showing great potential in AI.

In clinical practice, the artery pulse, as an important index of heart rate, aged or stiff blood vessel, and arterial blood pressure, provides extremely favorable information to diagnose potential cardiovascular disease with non-invasive medical method.[22] Excellent sensing performances of SPMSS, such as, ultralow detection limit (0.001%) and ultrafast response time (5 ms), provide the possibility for accurate pulse measurement. During the pulse waveform measurement, SPMSS is fixed on different arterial pulse positions of a healthy 24 years old male volunteer for health monitoring. As shown in Figure S30, Supporting Information, the pulse waveforms at the brachial, carotid, temporal, finger tips, clavicle, radial, posterior tibial, and dorsalis pedis artery are all measured in detail. Obviously, SPMSS is sensitive enough to exhibit different $\Delta R/R_0$ and pulse waveforms in various arterial pulse sites, which depends on the skin surface deflections attributed to the arterial pulse, further affects by the distance from heart, the compliance and depth of the arteries. Figure S31, Supporting Information, shows continuous and stable noninvasive pulse monitoring (400 s) of the radial artery, which is of great significance for long-term diagnosis of cardiovascular disease. Medical and physiological parameters acquired from arterial pulse waveforms are very useful and critical to evaluate health. In Figure 5d, the pulse waveforms of brachial and radial artery are precisely measured. Figure 5e shows that the radial artery possesses a typical pulse waveform with three characteristic peaks of percussion (P), tidal (T), and dicrotic (D) wave, and the corresponding pulse pressures include P_1, P_2, and P_3. According to the relative value of the P and T wave, the augmentation index (AIx) of the artery can be calculated by using the formula as follows:[23]

$$\mathrm{AIx}(\%) = \frac{P_2}{P_1} \times 100\% \tag{3}$$

Which is one of the significant parameters measuring the blood vessel stiffness. The AIx value of the radial artery is 60.2%, demonstrating that the volunteer in this study is a normal and healthy young male.[24] Besides, the periodic time as a unique parameters, including t_1, t_2, t_3, t_4, t_5, and t, is of great importance for experts to diagnose as well.[25] The pulse wave velocity (PWV), as another important parameter, is obtained through testing the pulse waveforms at various pulse positions. As an independent cardiovascular risk factor,[26] the PWV can reflect the degree of arterial stiffness in time.[27] As shown in Figure 5f, through recording each pulse waveform simultaneously, it is clearly observed that the brachial-radial arterial pulse has a time delay (Δt, or the pulse transmit time (PTT)).[28] Figure 5g illustrates the calculation formula of PWV as follows:[29]

$$\mathrm{PWV} = \frac{\Delta L}{\Delta t} \tag{4}$$

where ΔL represents the path length from a pulse position to another. By analyzing the as-acquired pulse waveforms,

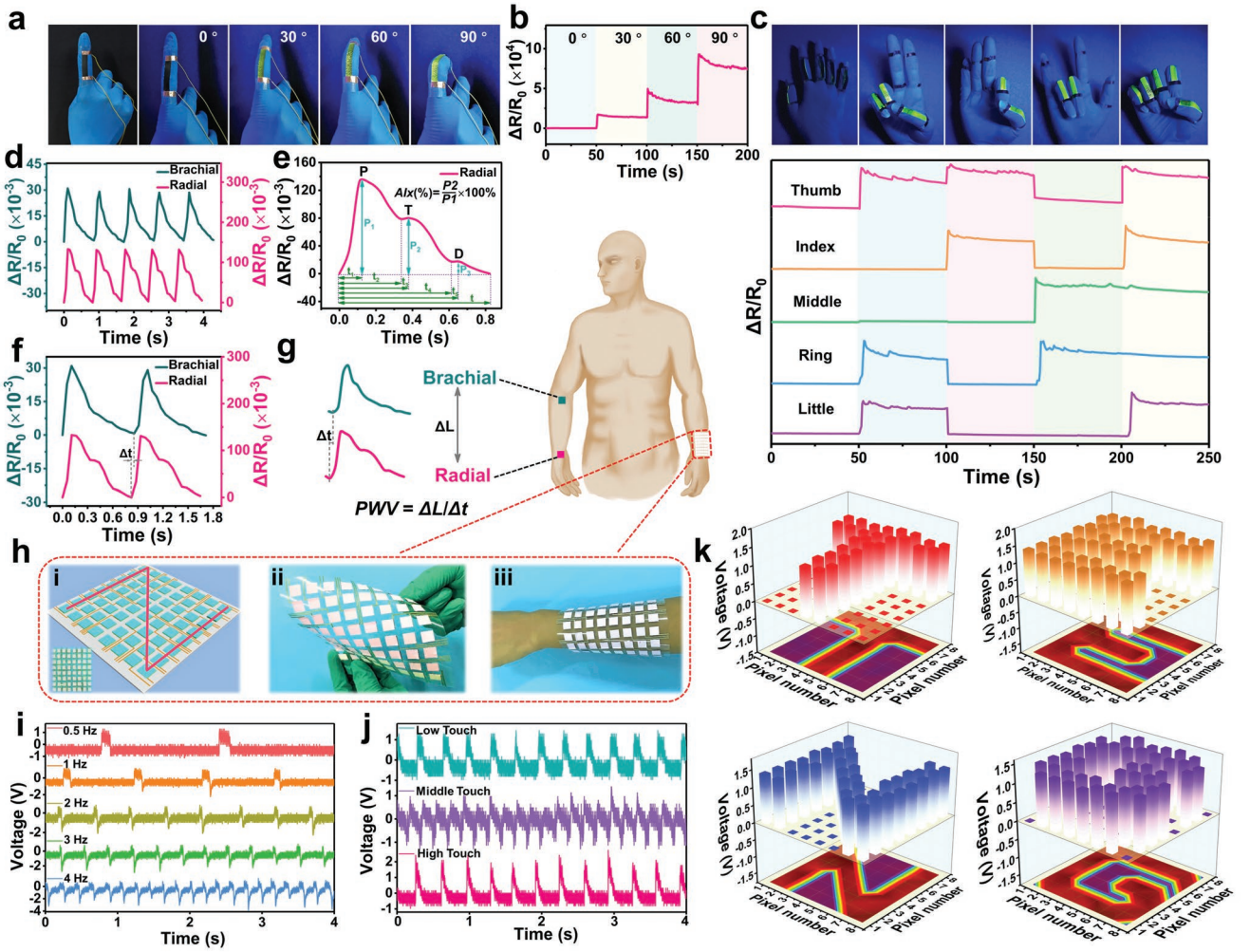

Figure 5. Applications of SPMSS in visual sensing, health monitoring and self-powered sensing. a) Photographs and b) $\Delta R/R_0$ of SPMSS integrated on the index finger excited by ML with different bending angles. c) Photographs and $\Delta R/R_0$ of SPMSS excited by ML with different gestures. d) The radial and brachial artery pulse waveforms. e) Characteristics of a radial artery pulse waveform. f) Enlarged view of (d) to show the PTT, Δt. g) The schematic diagram of PWV calculation. h) Schematic illustration of S-TENG based SPMSS array with 8 × 8 pixels. i) Output voltage of the single pixel (1×1 cm^2) of SPMSS array with various frequencies and j) pressures of finger touch. k) The movement trajectory of index finger and the output voltage mapping.

vital physiological and medical parameters are obtained: The average brachial-radial PTT is 33.2 ± 0.1 ms, and brachial-radial PWV (brPWV) is 7.5 m•s^{-1} (brachial-radial ΔL is 25 cm). The brPWV value demonstrates that our volunteer is a healthy young male,[30] in view of the brPWV threshold of 16.7 m•s^{-1} for arterial stiffness diagnosis.[31]

To solve the detection limitation of a single S-TENG based SPMSS in self-powered sensing applications and achieve comprehensive information, a self-powered SPMSS sensing array integrated with a group of single sensing units is developed, realizing a mapping of touch in 2D area. Figure S32, Supporting Information, and Figure 5h show schematic illustration of SPMSS array with 8 × 8 pixels, the SPMSS array is attached to the skin of a volunteer to sense finger touch and harvest the biomechanical energy. Figure 5i,j show that the output voltage of single SPMSS array pixel (1×1 cm^2) rises obviously with the increase of finger touch pressures and frequencies, exhibiting a good sense toward touch. As illustrated in Figure 5k, when a finger is placed on different contact position of the self-powered tactile sensing array, the output voltages of corresponding sensing units can be collected to precisely reveal the finger touch trajectory (T, E, N, and G, respectively). These results indicate that the self-powered sensing ability enables potential application of SPMSS as high performance smart skin.

3. Conclusion

In summary, we have successfully developed an ultrasensitive self-powered ML smart skin composed of a flexible TFM substrate and a synergistic conductive layer of MXene/CNT. Benefitting from the bioinspired structure design of strain-dependent microcrack, SPMSS demonstrates ultrasensitive sensing performances in a large strain range including ultralow detection

limit, ultrahigh sensitivity, and ultrafast response. SPMSS is also designed to be highly sensitive when exhibits ML property. These excellent abilities endow SPMSS with the ability of precisely monitoring health conditions by as-acquiring physiological parameters in real-time, and visually sensing different gestures through clearly distinguishable luminescent signals. Excellent TENG properties including ultrahigh triboelectric output and power density generate reliable power source supply to sustainably drive electronic devices. Besides, SPMSS is capable of working in S-TENG manner for self-powered sensing. SPMSS array is easily conformed to human skin, and can be used for harvesting biomechanical energy, tactile sensing, and spatial mapping on different desired objects. This study paves a new strategy for the fabrication of multifunctional smart skin with an all-in-one ability of high performance strain sensing, tunable optical characteristic and reliable power supply. The design and realization of our smart skin have broad potential applications in AI, human-machine interaction, and soft robots.

4. Experimental Section

The detailed experimental section can be found in the Supporting Information.

Supporting Information

Supporting Information is available from the Wiley Online Library or from the author.

Acknowledgements

Y.Z. and W.G. contributed equally to this work. The research was financially supported by National Natural Science Foundation of China (51773183, U1804133, U1604253), Henan Province University Innovation Talents Support Program (20HASTIT001), and Innovation Team of Colleges and Universities in Henan Province (20IRTSTHN002). The authors would also like to thank Prof. Zhifeng Shi from Zhengzhou University for their support on photoluminescence spectra measurements.

Conflict of Interest

The authors declare no conflict of interest.

Data Availability Statement

Research data are not shared.

Keywords

mechanoluminescence, strain sensors, triboelectric nanogenerators, visual sensors, $Ti_3C_2T_x$ (MXene)

Received: March 25, 2021
Revised: May 7, 2021
Published online: September 23, 2021

[1] a) A. Chortos, J. Liu, Z. Bao, *Nat. Mater.* **2016**, *15*, 937; b) D. Son, J. Kang, O. Vardoulis, Y. Kim, N. Matsuhisa, J. Oh, J. To, J. Mun, T. Katsumata, Y. Liu, A. McGuire, M. Krason, F. Molina-Lopez, J. Ham, U. Kraft, Y. Lee, Y. Yun, Z. B. J. Tok, *Nat. Nanotechnol.* **2018**, *13*, 1057; c) A. Chortos, Z. Bao, *Mater. Today* **2014**, *17*, 321.

[2] a) Y. Kim, A. Chortos, W. Xu, Y. Liu, J. Oh, D. Son, J. Kang, A. Foudeh, C. Zhu, Y. Lee, S. Niu, J. Liu, R. Pfattner, Z. Bao, T. Lee, *Science* **2018**, *360*, 998; b) E. Topol, *Nat. Med.* **2019**, *25*, 44; c) M. Segler, M. Preuss, M. Waller, *Nature* **2018**, *555*, 604; d) K. Dong, X. Peng, Z. L. Wang, *Adv. Mater.* **2020**, *32*, 1902549.

[3] D. Kang, P. Pikhitsa, Y. Choi, C. Lee, S. Shin, L. Piao, B. Park, K. Suh, T. Kim, M. Choi, *Nature* **2014**, *516*, 222.

[4] a) S. Park, S. Heo, W. Lee, D. Inoue, Z. Jiang, K. Yu, H. Jinno, D. Hashizume, M. Sekino, T. Yokota, K. Fukuda, K. Tajima, T. Someya, *Nature* **2018**, *561*, 516; b) F. Fan, W. Tang, Z. L. Wang, *Adv. Mater.* **2016**, *28*, 4283; c) X. Wang, Y. Zhang, X. Zhang, Z. Huo, X. Li, M. Que, Z. Peng, H. Wang, C. Pan, *Adv. Mater.* **2018**, *30*, 1706738; d) B. Zhang, Y. Tang, R. Dai, H. Wang, X. Sun, C. Qin, Z. Pan, E. Liang, Y. Mao, *Nano Energy* **2019**, *64*, 103953.

[5] a) J. Kim, A. Campbell, B. Ávila, J. Wang, *Nat. Nanotechnol.* **2019**, *37*, 389; b) S. Wang, J. Xu, W. Wang, G. Wang, R. Rastak, F. Molina-Lopez, J. Chung, S. Niu, V. Feig, J. Lopez, T. Lei, S. Kwon, Y. Kim, A. Foudeh, A. Ehrlich, A. Gasperini, Y. Yun, B. Murmann, J. Tok, Z. Bao, *Nature* **2018**, *555*, 83; c) Y. Tan, H. Godaba, G. Chen, S. Tan, G. Wan, G. Li, P. Lee, Y. Cai, S. Shepherd, J. Ho, B. Tee, *Nat. Mater.* **2019**, *19*, 7; d) W. Wu, X. Wang, X. Han, Z. Yang, G. Gao, Y. Zhang, J. Hu, Y. Tan, A. Pan, C. Pan, *Adv. Mater.* **2019**, *31*, 1805913.

[6] a) Y. Ma, Y. Yue, H. Zhang, F. Cheng, W. Zhao, J. Rao, S. Luo, J. Wang, X. Jiang, Z. Liu, N. Liu, Y. Gao, *ACS Nano* **2018**, *12*, 3209; b) X. Shi, H. Wang, X. Xie, Q. Xue, J. Zhang, S. Kang, C. Wang, J. Liang, Y. Chen, *ACS Nano* **2019**, *13*, 649; c) Y. Cai, J. Shen, G. Ge, Y. Zhang, W. Jin, W. Huang, J. Shao, J. Yang, X. Dong, *ACS Nano* **2018**, *12*, 56; d) Y. Yang, L. Shi, Z. Cao, R. Wang, J. Sun, *Adv. Funct. Mater.* **2019**, *29*, 1807882.

[7] a) Y. Ma, N. Liu, L. Li, X. Hu, Z. Zou, J. Wang, S. Luo, Y. Gao, *Nat. Commun.* **2017**, *8*, 1207; b) W. Cao, C. Ma, D. Mao, J. Zhang, M. Ma, F. Chen, *Adv. Funct. Mater.* **2019**, *29*, 1905898; c) Y. Yang, Z. Cao, P. He, L. Shi, G. Ding, R. Wang, J. Sun, *Nano Energy* **2019**, *66*, 104134; d) Y. Guo, M. Zhong, Z. Fang, P. Wan, G. Yu, *Nano Lett.* **2019**, *19*, 1143.

[8] A. Lipatov, M. Alhabeb, M. Lukatskaya, A. Boson, Y. Gogotsi, A. Sinitskii, *Adv. Electron. Mater.* **2016**, *2*, 1600255.

[9] a) C. Wu, S. Zeng, Z. Wang, F. Wang, H. Zhou, J. Zhang, Z. Ci, L. Sun, *Adv. Funct. Mater.* **2018**, *28*, 1803168; b) X. Qian, Z. Cai, M. Su, F. Li, W. Fang, Y. Li, X. Zhou, Q. Li, X. Feng, W. Li, X. Hu, X. Wang, C. Pan, Y. Song, *Adv. Mater.* **2018**, *30*, 1800291; c) B. Park, J. Kim, J. Kim, D. Tahk, C. Jeong, J. Ok, J. Shin, D. Kang, T. Kim, *Adv. Funct. Mater.* **2019**, *29*, 1903360.

[10] a) J. Wang, S. Li, F. Yi, Y. Zi, J. Lin, X. Wang, Y. Xu, Z. L. Wang, *Nat. Commun.* **2016**, *7*, 12744; b) Z. L. Wang, *Mater. Today* **2017**, *20*, 74; c) M. Wang, J. Zhang, Y. Tang, J. Li, B. Zhang, E. Liang, Y. Mao, X. Wang, *ACS Nano* **2018**, *6*, 6156; d) F. Peng, D. Liu, W. Zhao, G. Zheng, Y. Ji, K. Dai, L. Mi, D. Zhang, C. Liu, C. Shen, *Nano Energy* **2019**, *65*, 104068; e) Y. Tang, H. Zhou, X. Sun, N. Diao, J. Wang, B. Zhang, C. Qin, E. Liang, Y. Mao, *Adv. Funct. Mater.* **2020**, *30*, 1907893; f) G. Gao, B. Wan, X. Liu, Q. Sun, X. Yang, L. Wang, C. Pan, Z. L. Wang, *Adv. Mater.* **2018**, *30*, 1705088; g) C. Ning, L. Tian, X. Zhao, S. Xiang, Y. Tang, E. Liang, Y. Mao, *J. Mater. Chem. A* **2018**, *6*, 19143.

[11] S. Zeng, D. Zhang, W. Huang, Z. Wang, S. Freire, X. Yu, A. Smith, E. Huang, H. Nguon, L. Sun, *Nat. Commun.* **2016**, *7*, 11802.

[12] a) M. Lukatskaya, O. Mashtalir, C. Ren, Y. Dall'Agnese, P. Rozier, P. Taberna, M. Naguib, P. Simon, M. Barsoum, Y. Gogotsi, *Science* **2013**, *353*, 1137; b) M. Alhabeb, K. Maleski, B. Anasori, P. Lelyukh, L. Clark, S. Sin, Y. Gogotsi, *Chem. Mater.* **2017**, *29*, 7633.

[13] J. Yan, C. Ren, K. Maleski, C. Hatter, B. Anasori, P. Urbankowski, A. Sarycheva, Y. Gogotsi, *Adv. Funct. Mater.* **2017**, *27*, 1701264.
[14] C. Pang, G. Lee, T. Kim, S. Kim, H. Kim, S. Ahn, K. Suh, *Nat. Mater.* **2012**, *11*, 795.
[15] a) M. Zhang, C. Wang, H. Wang, M. Jian, X. Hao, Y. Zhang, *Adv. Funct. Mater.* **2017**, *27*, 1604795; b) S. Lee, S. Shin, S. Lee, J. Seo, J. Lee, S. Son, H. Cho, H. Algadi, S. Al-Sayari, D. Kim, T. Lee, *Adv. Funct. Mater.* **2015**, *25*, 3114; c) Y. Cai, J. Shen, Z. Dai, X. Zang, Q. Dong, G. Guan, L. Li, W. Huang, X. Dong, *Adv. Mater.* **2017**, *29*, 1606411; d) Q. Liu, J. Chen, Y. Li, G. Shi, *ACS Nano* **2016**, *10*, 7901.
[16] a) Z. Liu, D. Qi, G. Hu, H. Wang, Y. Jiang, G. Chen, Y. Luo, X. Loh, B. Liedberg, X. Chen, *Adv. Mater.* **2018**, *30*, 1704229; b) X. Shi, S. Liu, Y. Sun, J. Liang, Y. Chen, *Adv. Funct. Mater.* **2018**, *28*, 1800850; c) X. Li, R. Zhang, W. Yu, K. Wang, J. Wei, D. Wu, A. Cao, Z. Li, Y. Cheng, Q. Zheng, R. Ruoff, H. Zhu, *Sci. Rep.* **2012**, *2*, 870.
[17] a) X. Liu, C. Tang, X. Du, S. Xiong, S. Xi, Y. Liu, X. Shen, Q. Zheng, Z. Wang, Y. Wu, A. Horner, J. Kim, *Mater. Horiz.* **2017**, *4*, 477; b) C. Wang, X. Li, E. Gao, M. Jian, K. Xia, Q. Wang, Z. Xu, T. Ren, Y. Zhang, *Adv. Mater.* **2016**, *28*, 6640; c) X. Li, H. Hu, T. Hua, B. Xu, S. Jiang, *Nano Res.* **2018**, *11*, 5799.
[18] a) L. Lu, Y. Zhou, J. Pan, T. Chen, Y. Hu, G. Zheng, K. Dai, C. Liu, C. Shen, X. Sun, H. Peng, *ACS Appl. Mater. Interfaces* **2019**, *11*, 4345; b) T. Huang, P. He, R. Wang, S. Yang, J. Sun, X. Xie, G. Ding, *Adv. Funct. Mater.* **2019**, *29*, 1903732; c) Y. Cheng, R. Wang, J. Sun, L. Gao, *Adv. Mater.* **2015**, *27*, 7365.
[19] a) C. Wang, J. Zhao, C. Ma, J. Sun, L. Tian, X. Li, F. Li, X. Han, C. Liu, C. Shen, L. Dong, J. Yang, C. Pan, *Nano Energy* **2017**, *34*, 578; b) S. Wang, P. Xiao, Y. Liang, J. Zhang, Y. Huang, S. Wu, S. Kuo, T. Chen, *J. Mater. Chem. C* **2018**, *6*, 5140; c) Q. Sun, W. Seung, B. Kim, S. Seo, S. Kim, J. Cho, *Adv. Mater.* **2015**, *27*, 3411.
[20] a) Y. Yu, Y. Zhai, Z. Yun, W. Zhai, X. Wang, G. Zheng, C. Yan, K. Dai, C. Liu, C. Shen, *Adv. Electron. Mater.* **2019**, *5*, 1900538; b) Y. Zhou, P. Zhan, M. Ren, G. Zheng, K. Dai, L. Mi, C. Liu, C. Shen, *ACS Appl. Mater. Interfaces* **2019**, *11*, 7405.
[21] X. Peng, K. Dong, C. Ye, Y. Jiang, S. Zhai, R. Cheng, D. Liu, X. Gao, J. Wang, Z. Wang, *Sci. Adv.* **2020**, *6*, eaba9624.
[22] X. Wang, Z. Liu, T. Zhang, *Small* **2017**, *13*, 1602790.
[23] K. Kohara, Y. Tabara, A. Oshiumi, Y. Miyawaki, T. Kobayashi, T. Miki, *Am. J. Hypertens.* **2005**, *18*, 11.
[24] J. Sugawara, H. Komine, M. Yoshiwaza, T. Tarumi, S. Maeda, H. Tanaka, *Artery Res.* **2010**, *4*, 15.
[25] Y. Yim, K. Park, *J. Acupunct. Meridian Stud.* **2014**, *7*, 133.
[26] H. Obeid, V. Ouedraogo, M. Hallab, *J. Arch. Mil. Med.* **2017**, *5*, e13204.
[27] E. Messas, M. Pernot, M. Couade, *Diagn. Interventional Imaging* **2013**, *94*, 561.
[28] R. Smith, J. Argod, J. Pépin, P. Lévy, *Thorax* **1999**, *54*, 452.
[29] J. Weir-McCall, L. Brown, J. Summersgill, P. Talarczyk, M. Bonnici-Mallia, S. Chin, F. Khan, A. Struthers, F. Sullivan, H. Colhoun, A. Shore, K. Aizawa, L. Groop, J. Nilsson, J. Cockcroft, C. McEniery, I. Wilkinson, Y. Ben-Shlomo, J. Houston, *Hypertension* **2018**, *71*, 937.
[30] W. Rogers, Y. Hu, D. Coast, D. Vido, C. Kramer, R. Pyeritz, N. Reichek, *J. Am. Coll. Cardiol.* **2001**, *38*, 1123.
[31] Y. Cheng, Y. Li, C. Sheng, Q. Huang, J. Wang, *Pulse* **2015**, *3*, 253.